Atmos. Chem. Phys. Discuss., 13, 22607–22637, 2013
www.atmos-chem-phys-discuss.net/13/22607/2013/
doi:10.5194/acpd-13-22607-2013

Atmospheric Chemistry and Physics Discussions

On the presence of equatorial waves in the lower stratosphere of a general circulation model

P. Maury and F. Lott

Laboratoire de Météorologie Dynamique, UMR8539, IPSL, CNRS/ENS/UPMC/Ecole Polytechnique, Paris, France

Received: 21 May 2013 – Accepted: 5 August 2013 – Published: 30 August 2013

Correspondence to: P. Maury (pmaury@lmd.ens.fr)

Published by Copernicus Publications on behalf of the European Geosciences Union.

Abstract

To challenge the hypothesis that equatorial waves in the lower stratosphere are essentially forced by convection, we use the LMDz atmospheric model extended to the stratosphere and compare two versions having very different convection schemes but no quasi biennial oscillation (QBO). The two versions have realistic time mean precipitation climatologies but very different precipitation variabilities. Despite these differences, the equatorial stratospheric Kelvin waves at 50 hPa are almost identical in the two versions and quite realistic. The Rossby-gravity waves are also very close but significantly weaker than in observations. We demonstrate that this bias on the Rossby-gravity waves is essentially due to a dynamical filtering occurring because the model zonal wind is systematically westward: during a westward phase of the QBO, the Rossby-gravity waves in ERA-Interim compare well with those in the model.

These results suggest that in the model the effect of the convection scheme on the waves is in part hidden by the dynamical filtering and the waves are produced by other sources than equatorial convection. For the Kelvin waves, this last point is illustrated by an Eliassen and Palm flux analysis, showing that in the model they come more from the subtropics and mid-latitude regions whereas in the ERA-Interim reanalysis the sources are more equatorial. We also show that non-equatorial sources are significant in reanalysis data, and we consider the case of the Rossby-gravity waves. We identify situations in the reanalysis where here are large Rossby-gravity waves in the middle stratosphere, and for dates when the stratosphere is dynamically separated from the equatorial troposphere. We refer to this process as a "stratospheric reloading".

1 Introduction

In the equatorial stratosphere, the dominant modes of the synoptic scale variability are the Rossby-gravity waves (RGWs) and the Kelvin waves (KWs) first observed in soundings by Yanai and Maruyama (1966) and Wallace and Kousky (1968). These

ACPD
13, 22607–22637, 2013

planetary scale waves induce perturbations on the horizontal wind of a few meters per second and on temperature of a few Kelvin. These values are larger than the intra-seasonal standard deviation of these fields (Lott et al., 2009). The KWs and RGWs also contribute significantly to the forcing of the quasi-biennial oscillation (QBO) (Holton and Lindzen, 1972; Baldwin et al., 2001) and to the dehydration of the air at the tropical tropopause (Jensen et al., 2011; Fujiwara et al., 2001).

The stratospheric equatorial waves (SEWs) are generally considered to be forced by tropical convection (Manzini and Hamilton, 1993; Pires et al., 1997; Lindzen, 2003; Randel and Wu, 2005), and then to propagate freely above their convective sources. They are distinct from the convectively coupled equatorial waves (CCEWs) in the troposphere (Wheeler and Kiladis, 1999; Straub and Kiladis, 2003; Cho et al., 2004), which are slower than the SEWs and correspond to small vertical wavelengths in the stratosphere where they dissipate rapidly. Despite this difference, these two types of waves are sometimes related (Hendon and Wheeler, 2008) and stratospheric KWs often accompany the life cycle of convectively coupled KWs (Maury et al., 2011). This illustrates that the organisation of convection plays a role as shown by Garcia and Salby (1987) and Randel and Wu (2005), but there is today more and more evidence, that the filtering by the background flow largely affects the relationship between the stratospheric waves and their convective sources (Alexander and Ortland, 2010).

As the large scale equatorial waves can have small vertical wavelengths in the stratosphere, the general circulation models (GCMs) have difficulties in simulating some of them. This is critical for the RGWs with vertical wavelengths of a few kilometers (Boville and Randell, 1992). Also, the GCMs are inconsistent between them when it comes to represent the equatorial convection variability, and this can yield large differences on the resolved SEWs (Horinouchi et al., 2003). This result needs to be further analysed because the differences with the models in Horinouchi et al. (2003) are not just their convection schemes. In a complementary approach Ricciardulli and Garcia (2000) used only one model and showed that changes in the convection scheme strongly im-

ACPD
13, 22607–22637, 2013

pacts the KWs and RGWs. Nevertheless, the vertical resolution of the GCM used did not allow them to extend this result to the stratosphere.

The present paper analyses the equatorial waves in the LMDz-GCM (Hourdin et al., 2006) extended to the stratosphere (Lott et al., 2005) with two drastically different convection schemes, the Tiedtke (1989) and the Emanuel (1991) schemes. One important aspect of our work is that the two schemes have been used in CMIP experiments with LMDz and thus, they both have been tuned to provide realistic seasonal mean precipitation climatologies. As we will see, the intra-seasonnal precipitation variabilities are nevertheless very different. The novelty of the present work is that we can analyse the impact of these differences on SEWs in two simulations with realistic mean climatologies. We will show that the differences moderately impact the equatorial waves in the model stratosphere, which contradict the study of Horinouchi et al. (2003), at least concerning the planetary scale waves. This result is nevertheless consistent with Maury et al. (2011), where it is shown that the LMDz model simulates stratospheric KWs while its convective variability is underestimated. To interpret this result and to validate the SEWs in the model, we will then locate the sources of the waves in the model and determine if these sources are realistic.

The plan of the paper is as follows. Section 2 introduces the various datasets, and compares the precipitation variabilities between the two model versions and the observations. Section 3 presents a spectral analysis to characterise the precipitation variability and the presence of KWs and RGWs coupled to the convection. We then analyse the KWs and the RGWs in the lower stratosphere via a spectral analysis in Sect. 4, and a composite analysis in Sect. 5. To interpret the origin of the waves in the model, Sect. 6 presents Eliassen and Palm (1961) flux (EP-flux) diagnostics for the KWs. As the EP-flux appears to be quite small for the RGWs, Sect. 6 tries to interpret the origin of the RGWs in the model via a composite analysis from the reanalysis data using a different scenario. Section 7 summarises and discusses the results.

ACPD
13, 22607–22637, 2013

2 Datasets and precipitation climatologies

2.1 Model description and datasets

In this study we use the LMDz grid point model (Hourdin et al., 2006) extended to the stratosphere by Lott et al. (2005). In all the simulations analysed, the resolution in longitude is $\Delta\phi = 2.5^{\circ}$ and in latitude $\Delta\lambda = 3.75^{\circ}$. The model has 50 vertical levels, with a top at about 70 km, and a vertical resolution of about 1 km in the lower stratosphere and of about 2 km in the lower mesosphere. The model also includes orographic and non-orographic gravity waves drag (Lott and Miller, 1997; Hines, 1997) but does not simulate a QBO. A version with 80 vertical levels and a QBO also exists (Lott et al., 2012), but it has not been tested with the Tiedtke (1989) scheme. In this paper, LMDz is used with the two drastically distinct convection schemes due to Tiedtke (1989) and Emanuel (1991, 1993), where the model sensitivity to each parameterisation is described in Hourdin et al. (2006). For each scheme, a 20-yr long simulation is used, and we refer to each as LMDz-T and LMDz-E for the Tiedtke (1989) and Emanuel (1991, 1993) scheme respectively.

To validate our results, we use the daily precipitation from the Global Precipitation Climatology Project (GPCP) (Adler et al., 2003) over the period 1997–2008, and the daily horizontal wind and temperature from the ERA Interim (ERAI) reanalysis (Dee et al., 2011) over the period 1989–2009. We consider that the ERAI fields represent well the equatorial waves in the stratosphere, which is supported by comparison with satellite data for the temperature at zonal wavenumbers below $s = 10$ in Ern et al. (2008).

To characterise the convective activity we could have used the outgoing longwave radiation (OLR) datasets as done in many studies to cover a longer period than the GPCP data (e.g. Liebmann and Hartmann, 1982; Wheeler and Kiladis, 1999; Hendon and Wheeler, 2008). However, in LMDz we found that the OLR and the precipitation are not as well correlated as in observations, so we use here the precipitation, i.e. the more direct proxy of convective activity.

ACPD
13, 22607–22637, 2013

2.2 Precipitation climatologies

The seasonal means of precipitation are very similar and realistic in both simulations as expected since both schemes have been tuned for this purpose (not shown but see Hourdin et al., 2006). This is not the case for the precipitation variabilities as shown by Fig. 1, which represent the standard deviations of the precipitation calculated over six months during boreal summer and boreal winter. Figure 1a and d shows that in GPCP the variability is strong over the intertropical and south pacific convergence zones, and the monsoon regions as expected. Figure 1b and e shows that LMDz-E largely underestimates the convective variability in all these regions, whereas Fig. 1c and f shows that LMDz-T is more realistic when compared to GPCP (Fig. 1a and d).

3 The tropospheric equatorial waves

To characterise the space-time structure of the precipitation variability and to measure the contribution of the CCEWs, we next proceed to a spectral analysis of the precipitation fields (e.g. Wheeler and Kiladis (1999); Hendon and Wheeler (2008) or Lott et al. (2009) among others). For this purpose, we calculate the symmetric and antisymmetric means of the precipitation between the latitudes 10° S and 10° N. For a given X field, this consists in evaluating the quantities $X_s(\lambda,d,y)$ and $X_a(\lambda,d,y)$ (where the subscripts s and a denote symmetric and antisymmetric components) over N_ϕ latitudes,

$$\langle X_s\rangle(\lambda,d,y) = \frac{1}{N_\phi}\sum_{\phi=0}^{10^\circ N}\Big(X(\phi)+X(-\phi)\Big), \quad (1)$$

$$\langle X_a\rangle(\lambda,d,y) = \frac{1}{N_\phi}\sum_{\phi=0}^{10^\circ N}\Big(X(\phi)-X(-\phi)\Big). \quad (2)$$

ACPD
13, 22607–22637, 2013

To construct the spectra, we next subtract the annual cycle and then extract 360-day long segments, centered either on 1 July or on 1 January. To each segment we subtract the temporal trend and apply the tapered cosine window due to Tukey (1967). We then evaluate the segment's periodogram by performing a double Fourier transform in both longitude and time. Finally, the spectrum is estimated by averaging the periodograms over the years.

3.1 Results

To present the spectra, we use an energy conserving formalism where the spectra $S(s,\sigma)$ are multiplied by the frequency σ (in cycles per day), and are shown as a function of $\log(\sigma)$ and of the wavenumber s (e.g. Hendon and Wheeler, 2008; Maury et al., 2011). This semi-log representation and the use of equatorial averaged quantities, allow us to visualize the CCEWs signal due to KWs and RGWs without a normalisation by a red background as done by Wheeler and Kiladis (1999). The results are presented in Fig. 2 for the symmetric component and in Fig. 3 for the anti-symmetric component. We have also plotted on the spectra in Figs. 2 and 3 the theoretical dispersion curves of the equatorial waves deduced from the relation

$$\gamma^{1/2}(2\nu+1) = \gamma\sigma^2 - s^2 - \frac{s}{\sigma}, \tag{3}$$

where $\gamma = \dfrac{4a^2\Omega^2}{gh}$ is the Lamb parameter, a, Ω and g being the earth radius, the earth rotation rate and the gravity constant, respectively. In Eq. (3), the characteristic height h is related to the vertical wavenumber m by

$$m^2 = \frac{N^2}{gh} - \frac{1}{4H^2} \tag{4}$$

and the integer ν corresponds to the number of zeros of the meridional wind v between the poles. We impose the convention $\sigma > 0$, thus the sign of s provides the direction of

ACPD
13, 22607–22637, 2013

wave propagation, i.e. $s > 0$ ($s < 0$) for the eastward (westward) direction. For $\nu = -1$, only the solution $\sigma = s/\sqrt{\gamma}$ corresponding to the KWs needs to be considered.

3.1.1 Symmetric component

The power spectrum for the symmetric component of the GPCP precipitation in Fig. 2a is broadband in the two directions of propagation and shows enhanced power in the eastward direction for the periods between $\sigma^{-1} = 3$ days and $\sigma^{-1} = 10$ days and wavenumbers between $s = 3$ and $s = 10$. This corresponds to the convectively coupled KWs (CCKWs) signature found by Wheeler and Kiladis (1999). Still in the eastward direction, we also recognise the Madden–Julian oscillation spectral peak for wavenumbers $s = 1, 2$ and 3, and for periods between $\sigma^{-1} = 30$ days and $\sigma^{-1} = 50$ days. In the westward direction, the GPCP spectrum shows a relative maximum for wavenumbers between $s = -1$ and $s = -6$ and for periods $\sigma^{-1} \approx 15$–20 days, associated with the $\nu = 1$ convectively coupled equatorial Rossby waves (Wheeler and Kiladis, 1999). The black lines in Fig. 2a correspond to the dispersion curves from Eq. (3) with $\nu = -1$ for KWs (eastward direction) and with $\nu = 1$ for Rossby waves (westward direction). The dispersion curves that best match the maxima in the spectrum of these waves have equivalent depths in the range of about $h = 20$ m and $h = 50$ m, as expected for the CCEWs (Liebmann and Hendon, 1990; Wheeler and Kiladis, 1999).

The spectra in Fig. 2b and c shows that LMDz has difficulties in producing CCEWs, and especially in the eastward direction. More specifically, we can note that LMDz-T produces a small relative maximum for KWs with periods between $\sigma^{-1} = 8$ days and $\sigma^{-1} = 20$ days and wavenumbers between $s = 2$ and $s = 6$ (Fig. 2c), which is almost absent from LMDz-E (Fig. 2b). In the westward direction, the LMDz-T spectrum is stronger in amplitude than the LMDz-E spectrum, indicating that the equatorial Rossby waves are better simulated with the Tiedtke (1989) scheme. This difference will not be further analysed, since the equatorial Rossby waves are too slow to deeply penetrate in the stratosphere (Yang et al., 2011).

ACPD
13, 22607–22637, 2013

3.1.2 Antisymmetric component

The anti-symmetric GPCP precipitation spectrum in Fig. 3a is also broadband in the two directions but presents enhanced power from the wavenumber $s = -8$ and a period of about $\sigma^{-1} = 8$ days in the westward direction until the wavenumbers $s = 3$ in the eastward direction and a period of about $\sigma^{-1} = 3$ days. This region lies in the spectral domain of the convectively coupled RGWs (Wheeler and Kiladis, 1999), as indicated by the dispersion curves from Eq. (3) with $\nu = 0$, and for $h = 20$ m and $h = 50$ m. Figure 3b and c shows that LMDz-E largely underestimates the anti-symmetric precipitation variability, whereas LMDz-T is much more realistic in amplitude. Nevertheless, LMDz-T underestimates the eastward signal, and does not show enhanced power corresponding to RGWs. Another essential point with LMDz-T, and to a lesser extent with LMDz-E, is that the anti-symmetric spectra (Fig. 3b and c) have larger amplitude than the symmetric ones (Fig. 2b and c). This indicates that the precipitation variability is much less organised over the equator than in the observations and suggests that LMDz has difficulties in simulating a large-scale organisation of the convection, which might be due to the fact that the CCEWs are not well simulate.

4 Stratospheric spectra

To study the stratospheric equatorial waves, we use the fact that for the KWs and the RGWs, at least one of the dynamical fields u, v, T or Z, does not change sign within latitude in the equatorial band at a given longitude. In the following, the temperature (T) is used to characterise the KWs and the meridional wind (v) for the RGWs.

4.1 Temperature

The Fig. 4 shows the temperature spectra in the lower stratosphere at $z_p = 50$ hPa. The ERAI spectrum in Fig. 4a does not differ from the ERA40 spectra presented in Lott et al. (2009), and consists of a broad maximum for wavenumbers between $s = 1$ and $s = 5$

ACPD
13, 22607–22637, 2013

for periods between $\sigma^{-1} = 3$ days and $\sigma^{-1} = 20$ days, which corresponds to the KWs packets. This spectral peak occurs at slightly higher equivalent depths than the one attributed to convectively coupled KWs in Fig. 2a. This shift to higher equivalent depths in the stratosphere means that the vertical wavenumber of KWs decreases when the equivalent depth h increases and the corresponding KWs are less attenuated (see Eq. 4).

Figure 4b and c shows that spectra from the model are quite realistic and even larger in amplitude than those from ERAI. This occurs despite the much reduced amplitude of the precipitation spectra in the model, especially in the domain of the convectively coupled KWs. To understand this large wave signal, we must mention that the zonal mean zonal wind is always negative in the LMDz lower equatorial stratosphere (not shown, but the model does not simulate a QBO) whereas it is negative less than half of the time in observations. In the model stratosphere, the KWs always propagate easily as they have positive phase speed and hence larger positive intrinsic phase speed than during a null or positive zonal mean wind. This corroborates Alexander and Ortland (2010), which have shown that the filtering by the zonal wind strongly modulates the relationship between convection and stratospheric waves. Also, from the fact that in LMDz-E the zonal mean zonal wind is more negative than in LMDz-T (not shown), it follows that the KWs are stronger in LMDz-E than in LMDz-T.

4.2 Meridional wind

The Fig. 5 presents the meridional wind spectra in the lower stratosphere at $z_p =$ 50 hPa. The ERAI spectrum in Fig. 5a is dominated by a broad maximum in the westward direction between the wavenumbers $s = -4$ and $s = -8$ and the periods $\sigma^{-1} = 2$ days and $\sigma^{-1} = 8$ days, due to the RGWs packets (see Lott et al. (2009) and also the dispersion curves for RGWs calculated from Eq. (3) with $\nu = 0$). Once again, the equivalent depth associated with these waves is higher than for the RGWs in the troposphere. Figure 5b and c shows that the RGWs signal is largely underestimated

ACPD
13, 22607–22637, 2013

by LMDz, which is again more related to a dynamical filtering than to a deficiency in precipitation variability. Accordingly, the LMDz zonal wind zonal mean is negative in the upper troposphere and lower stratosphere implying that the RGWs packets with negative phase speed are more dissipated than in ERAI. The dominant role of the dynamical filtering is further illustrated by the larger RGWs signal in LMDz-T than in LMDz-E according to the more negative zonal wind in LMDz-E than in LMDz-T and despite the larger precipitation variability in LMDz-T than in LMDZ-E.

5 Composite analysis

To characterise the wave patterns we conduct the composite analysis described in Lott et al. (2009).

5.1 Kelvin waves

To extract the KWs packets, we apply to all fields (u, v, T and Φ) a large band-pass filter defined in the spectral domain, which essentially keeps the eastward propagating disturbances with frequency between $\sigma^{-1} = 3$ days and $\sigma^{-1} = 10$ days and wavenumbers between $s = 1$ and $s = 6$. This filter largely covers the maximum identified in the temperature spectrum at $z_p = 50$ hPa (Fig. 4). To detect the presence of the KWs packets at 50 hPa, we construct an index corresponding to the maximum value of the filtered temperature averaged between 10° S and 10° N at a given time. Then, the composites are built from dates selected when the index presents a maximum that exceeds a given threshold, chosen such that the number of dates selected equals the number of years in the dataset.

The composites for the winds and the temperature in Fig. 6 confirm that we are in the presence of KWs, since (i) the wind perturbations are almost exactly zonal and in quadrature with the temperature perturbations, and (ii) these signals are confined to the equatorial region. Figure 6 also shows that the peak in KWs amplitude is larger in

ACPD
13, 22607–22637, 2013

the model (Fig. 6b and c) than in ERAI (Fig. 6a), and even slightly larger in LMDz-E than in LMDz-T. As mentioned in Sect. 3, this is consistent with the fact that the dynamical filtering dominates, the zonal wind in the LMDz-E lower stratosphere being more negative than in LMDZ-T. In ERAI a filtering by the QBO is also active, since the selected dates occur during the easterly phases of the QBO at 50 hPa. Still during these easterly phases, the winds in ERAI are less negative than in both model simulations, which might explain the smaller amplitude in ERAI composites than in LMDz. As in Lott et al. (2009) and Maury et al. (2011), we also find that the absence of a QBO favours the KWs packets propagation up to the upper stratosphere, whereas the waves packets in ERAI are attenuated in the region where the QBO signal is eastward (not shown).

5.2 Rossby-gravity waves

To extract the RGWs, we apply to all fields a filter which essentially keeps the westward propagating disturbances with frequencies between $\sigma^{-1} = 3$ days and $\sigma^{-1} = 8$ days and wavenumbers between $s = 4$ and $s = 6$. Once again, this filter largely covers the maxima identified in the meridional wind spectra at $z_p = 50$ hPa (Fig. 5). To build the index we then use the meridional wind averaged between 10° S and 10° N.

The composites of the winds, from ERAI in Fig. 7a and from LMDz-E in Fig. 8a, confirm that we are in the presence of RGWs, since they present a succession of clockwise and anti-clockwise circulation centers, (i) centered at the equator and (ii) confined within the equatorial region. The RGWs packets in ERAI (Fig. 7a) are larger than in LMDz-E (Fig. 8a) or LMDz-T (not shown, but the composites are almost identical to those in Fig. 8a). As a first guess, we could attribute the deficit in RGWs in the model to a misrepresentation of the precipitation variability (see Figs. 2 and 3). Again, several pieces of evidence indicates that the background flow dynamically filters these waves. The first one is given by the longitude-time plots in Figs. 7b and 8b, which show that the negative absolute phase speed of the waves in LMDz is larger in amplitude than in ERAI. In the model, the absolute phase speed of the RGWs needs to be larger to maintain a subsequent negative intrinsic phase speed when the background zonal

ACPD
13, 22607–22637, 2013

wind is negative. The second one is given by the zonal-vertical profiles of the waves in Figs. 7c and 8c, which show that the vertical wavelength of the RGWs packet is smaller in the model than in ERAI and likely too small to properly resolve these waves. A final piece of evidence is provided by a composite analysis made with the ERAI datasets, where we only extract the RGWs during a negative phase of the QBO at 50 hPa. The resulting composites, presented in Fig. 9, strongly resemble those from LMDz in Fig. 8.

6 On the origin of the equatorial waves in the model

The above results indicate that there are realistic stratospheric RGWs and KWs in LMDz, despite the underestimation of the precipitation variability in the corresponding wavenumber-frequency window. This suggests that there exist other sources than equatorial convection for those waves, and that these sources can be substantial enough to supplement the lack of convective forcing.

6.1 EP-fluxes due to Kelvin waves composite

To locate these sources for the KWs, we next evaluate the EP-flux (Eliassen and Palm, 1961) vector $\overline{F}$ averaged over the dates selected to build the composites in Fig. 6, where

$$\overline{F^{\phi}} = \rho_0 a \cos\phi \left(\overline{u}_z \frac{\overline{v'\theta'}}{\overline{\theta}_z} - \overline{u'v'} \right) \quad (5)$$

$$\overline{F^{z}} = \rho_0 a \cos\phi \left(\left(f - \frac{(\overline{u}\cos\phi)_{\phi}}{a\cos\phi} \right) \frac{\overline{v'\theta'}}{\overline{\theta}_z} - \overline{u'w'} \right) \quad (6)$$

In Eqs. (5) and (6), u', v' and w' refer to the filtered perturbations of the three components of the wind and θ' is the composite perturbation of the potential temperature. The overbar corresponds to the zonal average for the wind ($\overline{u}$) and the potential tempera-

ACPD
13, 22607–22637, 2013

ture ($\overline{\theta}$), which are evaluated from the unfiltered fields. For completeness, the reference density is $\rho_0(z) = \rho_r \exp\left(-z/H\right)$ where ρ_r is a constant and the Coriolis parameter $f = 2\Omega \sin\phi$, where ϕ is the latitude.

The EP-flux vector $(\overline{F^z}, \overline{F^\phi})$ and its vertical component $\overline{F^z}$, are presented in Fig. 10. In the reanalysis (Fig. 10a), the EP-flux essentially comes from the mid-and-high troposphere of the equatorial regions, between 10° S and 10° N and above 8 km typically. The EP-flux is almost constant up to 15–17 km, suggesting that the KWs packet propagates with little dissipation from the upper troposphere to the lower stratosphere. The amplitude decreases rapidly above 18 km when the KWs dissipate. As observed in LMDz-E (Fig. 10b) and LMDz-T (Fig. 10c), the results from the model are very different, with the KWs EP-flux coming from regions around 15–20° S, that are significantly outside from the equatorial regions. This interpretation of the convection not being the main driver is also supported by the fact that the dates used to build Fig. 10 are selected during boreal summer, e.g. when the convection is stronger in the Northern Hemisphere subtropics, whereas the KWs seem to come from the southern subtropics, e.g. where the mid-latitudes synoptic variability is the strongest.

6.2 Rossby-gravity waves: stratospheric reloading

We tried to conduct a comparable analysis for the RGWs, but the EP-flux composites from the model are not significant enough to be conclusive. Note that this smallness of the vertical EP-flux is partly an intrinsic difficulty of the westward propagating RGWs that behave as Rossby waves. As a consequence, the RGWs vertical EP-flux is essentially related to the meridional heat flux term multiplied by the Coriolis parameter (see Eq. 6), implying that the vertical EP-flux becomes small near the equator for these waves.

To circumvent this problem, and illustrate that the extra-tropical forcing can be significant for the RGWs, we do as in Sect. 5 and build a scenario where such a forcing operates in the reanalysis. For this purpose we next evaluate a RGWs' composite at

ACPD
13, 22607–22637, 2013

20 hPa, in a configuration where the zonal wind is negative below this level. We know from the results in Sect. 5.2 that, during the negative phase of the QBO the RGWs can not reach 30 hPa (see Fig. 9c). Accordingly, we consider that the RGWs present at 20 hPa during such a phase of the QBO are dynamically separated from their convective sources in the troposphere. Figure 11a shows the horizontal wind (u', v') at the lag $l = 0$ day and at 20 hPa. We recognize the horizontal wind structure characteristic of RGWs, with wind maxima of about 4 m s^{-1}. The Hovmöller diagram on Fig. 11b indicates that the waves propagate westward with a phase speed $c_\phi \approx -19$ m s^{-1}, which is comparable to the RGWs phase speed at 50 hPa in Sect. 5.2. Finally, the vertical structure of the RGWs composite in Fig. 11c shows that the phase lines are slightly tilted eastward, which seems to indicate a downward propagation of these waves packets, rejecting the hypothesis that these RGWs come from below. This either calls for an external forcing from the mid-latitudes, as for the KWs in Sect. 6.1, or an internal dynamical mechanism within the equatorial jet.

7 Summary and discussion

The analysis of KWs and RGWs in the lower equatorial stratosphere of the LMDz GCM shows that this model overestimates the KWs and underestimates the RGWs in comparison with the ERAI reanalysis. This result is essentially due to a filtering effect, since the zonal mean zonal wind in the LMDz lower equatorial stratosphere is always negative. On the one hand, this favours the propagation of waves with positive phase speed (like the KWs), but on the other hand this disadvantages the propagation of waves with negative phase speed (like the RGWs).

It seems that for the large-scale waves we analyse, the dominant role of the background flow filtering almost completely tempers the impact of the convection scheme documented in Horinouchi et al. (2003) for instance. In fact, we use a LMDz simulation with a convection scheme producing a large precipitation variability (the Tiedtke (1989) scheme) and a simulation with a convection scheme producing a much smaller one

ACPD
13, 22607–22637, 2013

(the Emanuel (1993) scheme). We found that both versions resolve comparable large-scale equatorial waves in the lower stratosphere, which can be explained by at least two reasons. The first one follows Maury et al. (2011), which have shown that in reality stratospheric KWs sometimes accompany the life-cycle of CCKWs in the troposphere. When this mechanism is absent in models, the forcing of large scale waves by convection is inherently reduced. To a certain extent, one needs the convectively coupled waves to inject variability in the spectral domain where the large scale equatorial waves can propagate in the stratosphere. This suggests that the differences in precipitation variability are only important if they appear in the spectral space of the SEWs, but this idea could not be tested. The second reason might be due to the fact that the waves in the model have other sources, like for instance the subtropics and the mid-latitudes.

For the KWs, we corroborated this last point by an analysis of EP-fluxes, which illustrates that the LMDz sources originate rather from the subtropics and the mid-latitudes. The analysis of the RGWs EP-fluxes is more problematic, and could be explained by at least two reasons. Firstly, the RGWs in the model are weak and have life cycles different from those observed and secondly, the vertical component of the EP-flux for Rossby-like waves is very small near the equator. To circumvent these two issues we verified that the RGWs in the model are realistic by comparing them to composites from ERAI done during easterly phases of the QBO. To show that mid-latitude sources can also be effective for the RGWs, we used ERAI to make composites of the RGWs at 20 hPa with a positive zonal wind at this level and a negative one below. In such a situation, the presence of critical levels below 20 hPa filters the ascending waves, whereas the positive wind at 20 hPa favours their development, and we find again substantial RGWs. These RGWs necessarily come from the subtropics and mid-latitudes, or they are internally generated.

Although our results contradict the common view that in models the SEWs are forced by the convection, we recall that we only looked at the rather large scale waves that dominate the day-to-day variability and not at the entire equatorial wave spectrum. Also, in the model analysed the variability in the tropical troposphere is almost devoid

ACPD
13, 22607–22637, 2013

of CCEWs. These two limitations call for an extension of our methods to faster waves and to model versions that better simulate the CCEWs. Some of the CMIP5 models could be used to address this last issue.

Acknowledgements. We thank Elisa Manzini, Joan Alexander, and Richard Lindzen for helpful comments and Feedbacks. GPCP Precipitation data are provided by the NOAA/OAR/ESRL PSD, Boulder, Colorado, USA, from their Web site at http://www.esrl.noaa.gov/psd/. This work was supported by the FP7 EU-projects EMBRACE (Grant agreement 282672), and COMBINE (Grant agreement 226520).

The publication of this article is financed by CNRS-INSU.

References

Adler, R., Huffman, G. J., Chang, A., Ferraro, R., Xie, P.-P., Janowiak, J., Rudolf, B., Schneider, U., Curtis, S., Bolvin, D., Gruber, A., Susskind, J., Arkin, P., and Nelkin, E.: The version 2 Global Precipitation Climatology Project (GPCP) monthly precipitation analysis (1979–present), J. Hydrometeor., 4, 1147–1167, 2003. 22611

Alexander, M. J. and Ortland, D. A.: Equatorial waves in High Resolution Dynamics Limb Sounder HIRDLS data, J. Geophys. Res., 115, D24111, doi:10.1029/2010JD014782, 2010. 22609, 22616

Baldwin, M. P., Gray, L. J., Dunkerton, T. J., Hamilton, K., Haynes, P. H., Randel, W. J., Holton, J. R., Alexander, M. J., Hirota, I., Horinouchi, T., Jones, D. B. A., Kinnersley, J. S., Marquardt, C., Sato, K., and Takahashi, M.: The quasi-biennial oscillation, Rev. Geophys., 39, 179–229, 2001. 22609

Boville, B. A. and Randell, W. R.: Equatorial waves in a stratospheric GCM: effects of vertical resolution, J. Atmos. Sci., 49, 785–8001, 1992. 22609

ACPD

13, 22607–22637, 2013

Cho, H.-K., Bowman, K., and North, G.: Equatorial waves including the Madden–Julian oscillation in TRMM rainfall and OLR data, J. Climate, 17, 4387–4406, 2004. 22609

Dee, D. P., Uppala, S. M., Simmons, A. J., Berrisford, P., Poli, P., Kobayashi, S., Andrae, U., Balmaseda, M. A., Balsamo, G., Bauer, P., Bechtold, P., Beljaars, A. C. M., van de Berg, L., Bidlot, J., Bormann, N., Delsol, C., Dragani, R., Fuentes, M., Geer, A. J., Haimberger, L., Healy, S. B., Hersbach, H., Hólm, E. V., Isaksen, L., Kållberg, P., Köhler, M., Matricardi, M., McNally, A. P., Monge-Sanz, B. M., Morcrette, J.-J., Park, B.-K., Peubey, C., de Rosnay, P., Tavolato, C., Thépaut, J.-N., and Vitart, F.: The ERA-Interim reanalysis: configuration and performance of the data assimilation system, Q. J. Roy. Meteor. Soc., 137, 553–597, doi:10.1002/qj.828, 2011. 22611

Eliassen, A. and Palm, E.: On the transfer of energy in stationary moutain waves, Geofys. Publ., 22, 1–23, 1961. 22610, 22619

Emanuel, K.: A scheme for representing cumulus convection in large-scale models, J. Atmos. Sci., 48, 2313–2335, 1991. 22610, 22611

Emanuel, K.: A cumulus representation based on the episodic mixing model: the importance of mixing and microphysics in predicting humidity, AMS Meteorol. Monogr., 46, 185–194, 1993. 22611, 22622

Ern, M., Preusse, P., Krebsbach, M., Mlynczak, M. G., and Russell III, J. M.: Equatorial wave analysis from SABER and ECMWF temperatures, Atmos. Chem. Phys., 8, 845–869, doi:10.5194/acp-8-845-2008, 2008. 22611

Fujiwara, M., Hasebe, F., Shiotani, M., Nishi, N., Voemel, H., and Oltmans, S. J.: Water vapor control at the tropopause by equatorial Kelvin waves observed over the Galapagos, Geophys. Res. Lett., 28, 3143–3146, 2001. 22609

Garcia, R. R. and Salby, M. L.: Transient response to localized episodic heating in the tropics, Part II: Far-field behavior, J. Atmos. Sci., 44, 499–530, 1987. 22609

Hendon, H. and Wheeler, M.: Some space-time spectral analysis of tropical convection and planetary scale waves, J. Atmos. Sci., 65, 2936–2948, 2008. 22609, 22611, 22612, 22613

Hines, C. O.: Doppler spread parameterization of gravity wave momentum deposit in the middle atmosphere, Part I: Basic formulation, J. Atmos. Solar Terr. Phys., 59, 371–386, 1997. 22611

Holton, J. and Lindzen, R. S.: An updated theory for the quasi-biennial cycle in the tropical stratosphere, J. Atmos. Sci., 29, 1076–1080, 1972. 22609

ACPD
13, 22607–22637, 2013

On the presence of equatorial waves in the lower stratosphere

P. Maury and F. Lott

Horinouchi, T., Pawson, S., Shibata, K., Manzini, E., Giorgetta, M., and Sassi, F.: Tropical cumulus convection and upward propagating waves in middle-atmospheric GCMs, J. Atmos. Sci., 60, 2765–2782, 2003. 22609, 22610, 22621

Hourdin, F., Musat, I., Bony, S., Braconnot, P., Codron, F., Dufresne, J.-L., Fairhead, L., Filiberti, M.-A., Friedlingstein, P., Grandpeix, J.-Y., Krinner, G., LeVan, P., Li, Z.-X., and Lott, F.: The LMDz4 general circulation model: Climate performance and sensitivity to parametrized physics with emphasis on tropical convection, Clim. Dynam., 27, 787–813, doi:10.1007/s00382-006-0158-0, 2006. 22610, 22611, 22612

Jensen, E. J., Ackerman, A. S., Tabazadeh, A., and Toon, O. B.: A conceptual model of the dehyfration of air due to freeze-dryingby opticallt thin laminar cirrus rising slowly across the tropical tropopause, J. Geophys. Res., 106, 17237–17252, 2011. 22609

Liebmann, B. and Hartmann, D. L.: Interannual variations of outgoing IR associated with tropical circulation changes during 1974-1978 equator, J. Atmos. Sci., 39, 1153–1162, 1982. 22611

Liebmann, B. and Hendon, H. H.: Synoptic-scale disturbances near the equator, J. Atmos. Sci., 47, 1463–1479, 1990. 22614

Lindzen, R. S.: The interaction of waves and convection in the tropics, J. Atmos. Sci., 60, 3009–3020, 2003. 22609

Lott, F. and Miller, M.: A new subgrid scale orographic drag parameterization its testing in the ECMWF model, Q. J. Roy. Meteor. Soc., 123, 101–127, 1997. 22611

Lott, F., Fairhead, L., Hourdin, F., and Levan, P.: The stratospheric version of LMDz: dynamical climatologies, Arctic oscillation, and impact on the surface climate, Clim. Dynam., 25, 851–868, doi:10.1007/s00382-005-0064-x, 2005. 22610, 22611

Lott, F., Kuttippurath, J., and Vial, F.: A climatology of the gravest waves in the equatorial lower and middle stratosphere: method and results for the ERA-40 re-analysis and the LMDz GCM, J. Atmos. Sci., 66, 1327–1346, doi:10.1175/2008JAS2880.1, 2009. 22609, 22612, 22615, 22616, 22617, 22618

Lott, F., Guez, L., and Maury, P.: A stochastic parameterization of non-orographic gravity waves: formalism an impact on the equatorial stratosphere, Geophys. Res. Lett., 39, L06807, doi:10.1029/2012GL051001, 2012. 22611

Manzini, E. and Hamilton, K.: Middle atmospheric traveling waves forced by latent and convective heating, J. Atmos. Sci., 50, 2180–2200, 1993. 22609

ACPD
13, 22607–22637, 2013

Maury, P., Lott, F., Guez, L., and Duvel, J.-P.: Tropical variability and stratospheric equatorial waves in the IPSLCM5 model, Clim. Dynam., 40, 2331–2344, doi:10.1007/s00382-011-1273-0, 2011. 22609, 22610, 22613, 22618, 22622

Pires, P., Redelsperger, J. L., and Lafore, J. P.: Equatorial atmospheric waves and their association to convection, Mon. Weather Rev., 127, 1167–1184, 1997. 22609

Randel, W. J. and Wu, F.: Kelvin wave variability near the equatorial tropopause observed in GPS radio occultation measurements, J. Geophys. Res., 110, D03102, doi:10.1029/2004JD005006, 2005. 22609

Ricciardulli, L. and Garcia, R.: The excitation of equatorial waves by deep convection in the NCAR Community Climate Model CCM3, J. Atmos. Sci., 57, 3461–3487, 2000. 22609

Scinocca, J. F. and McFarlane, N. A.: The variability of modeled tropical precipitation, J. Atmos. Sci., 61, 1993–2015, 2004.

Straub, K. H. and Kiladis, G. N.: Extratropical forcing of convectively coupled Kelvin waves during austral winter, J. Atmos. Sci., 60, 526–543, 2003. 22609

Tiedtke, M.: A comprehensive mass flux scheme for cumulus parameterization in large-scale models, Mon. Weather Rev., 117, 1779–1800, 1989. 22610, 22611, 22614, 22621

Tukey, J. W.: An introduction to the calculations of numerical spectrum analysis, Spectr. Anal. Time Ser., 25–46, 1967 22613

Wallace, J. M. and Kousky, V. E.: Observational evidence of Kelvin waves in the tropical stratosphere, J. Atmos. Sci., 25, 900–907, 1968. 22608

Wheeler, M. and Kiladis, G.: Convectively coupled equatorial waves: analysis of clouds and temperature in the wavenumber-frequency domain, J. Atmos. Sci., 56, 374–399, 1999. 22609, 22611, 22612, 22613, 22614, 22615

Yanai, M. and Maruyama, T.: Stratospheric wave disturbances propagating over the equatorial Pacific, J. Meteor. Soc. Japan, 44, 291–294, 1966. 22608

Yang, G., Hoskins, B., and Slingo, J.: Equatorial waves in opposite QBO phases, J. Atmos. Sci., 68, 839–862, doi:10.1175/2010JAS3514.1, 2011. 22614

ACPD
13, 22607–22637, 2013

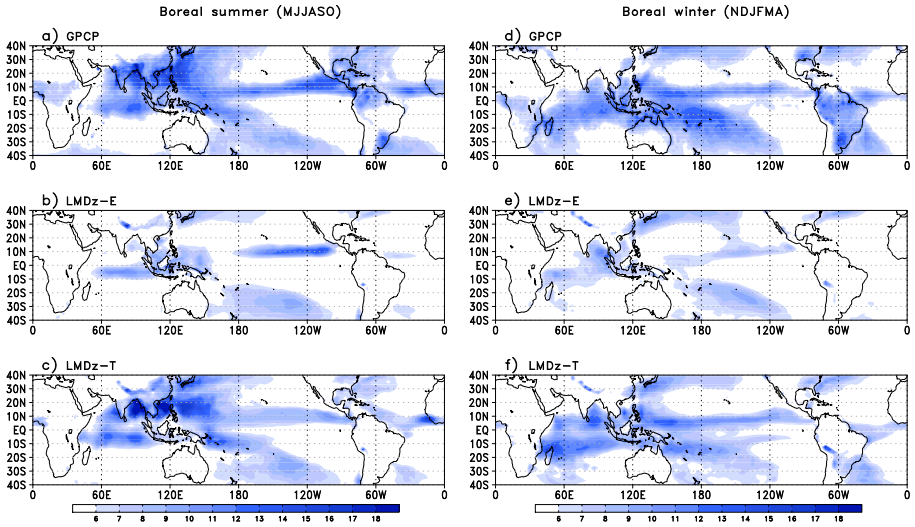

Fig. 1. Standard deviations of precipitation (mm day^{-1}) in boreal summer (March to August: MAMJJA, left panels) and boreal winter (September to February: SONDJF, right panels): **(a–d)** GPCP, **(b–e)** LMDz-E and **(c–f)** LMDz-T.

ACPD
13, 22607–22637, 2013

On the presence of equatorial waves in the lower stratosphere

P. Maury and F. Lott

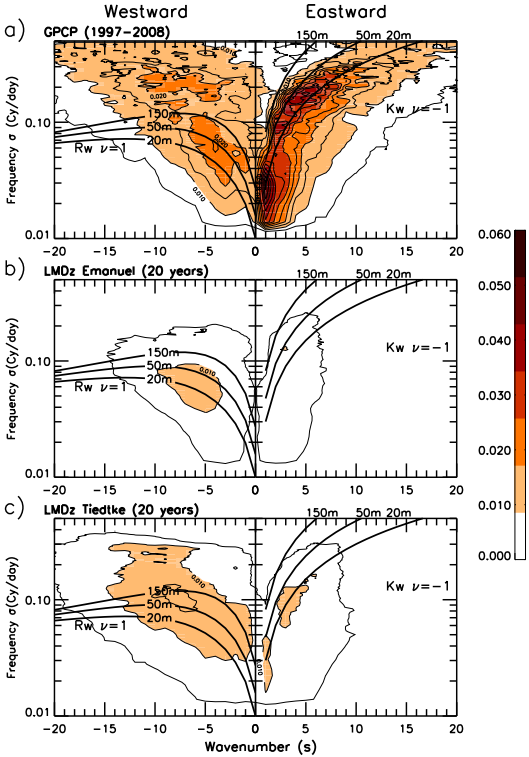

Fig. 2. Wavenumber-frequency spectra of the symmetric component of the precipitation averaged over the latitudes 10° S and 10° N (units are in $mm^2\,day^{-2}\,Cy\,day^{-1}$): **(a)** GPCP, **(b)** LMDz-E, and **(c)** LMDz-T. The interval between the thin solid lines is two times smaller than between the shaded areas. The superimposed dispersion curves (thick solid lines) are calculated from Eq. (3) for the KWs (with $\nu = -1$) in the eastward panels and for the Rossby waves (with $\nu = +1$) in the westward panels. They are displayed for the three equivalent depths $h = 20, 50$ and 150 m.

ACPD
13, 22607–22637, 2013

On the presence of equatorial waves in the lower stratosphere

P. Maury and F. Lott

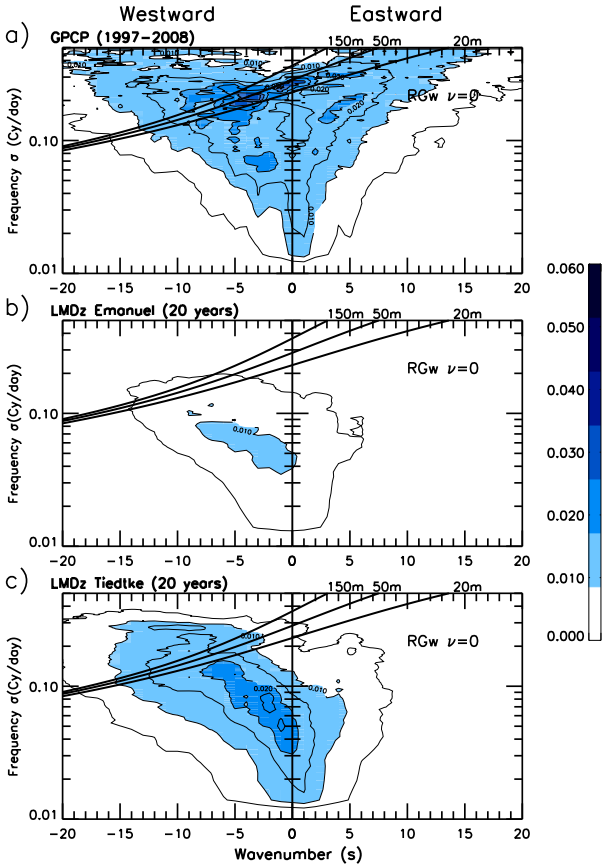

Fig. 3. Same as Fig. 2 except for the anti-symmetric component of precipitation. The dispersion curves are calculated for the RGWs (with $\nu = 0$).

ACPD
13, 22607–22637, 2013

On the presence of equatorial waves in the lower stratosphere

P. Maury and F. Lott

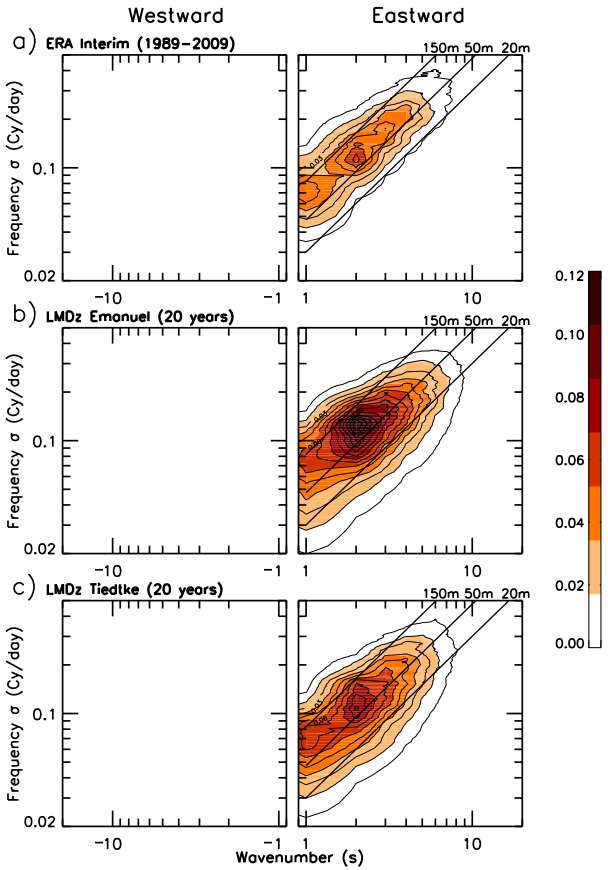

Fig. 4. Wavenumber-frequency spectra of the temperature averaged over the latitudes 10° S and 10° N, at 50 hPa (units are in $K^2\,Cy\,day^{-1}$): **(a)** ERAI, **(b)** LMDz-E and **(c)** LMDz-T. The interval between the thin solid lines is two times smaller than between the shaded areas. The dispersion curves (thick solid lines) from Eq. (3) are calculated for KWs ($\nu = -1$) with $h = 20, 50$ and 150 m.

ACPD
13, 22607–22637, 2013

On the presence of equatorial waves in the lower stratosphere

P. Maury and F. Lott

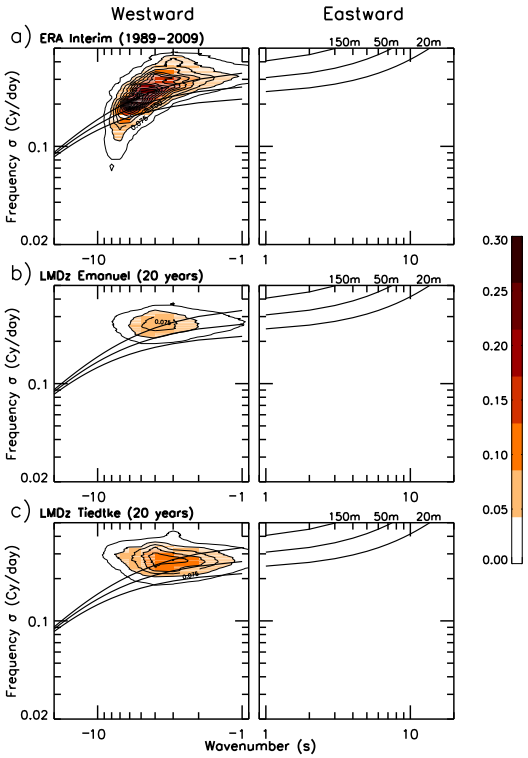

Fig. 5. Wavenumber-frequency spectra of the meridional wind averaged over the latitudes 10° S and 10° N, at 50 hPa (units are in $m^2 s^{-2}$ Cy day^{-1}): **(a)** ERAI, **(b)** LMDz-E and **(c)** LMDz-T. The interval between the thin solid lines is two times smaller than between the shaded areas. The dispersion curves (thick solid lines) from Eq. (3) are calculated for the RGWs ($\nu = 0$) with $h = 20, 50$ and 150 m.

ACPD
13, 22607–22637, 2013

On the presence of equatorial waves in the lower stratosphere

P. Maury and F. Lott

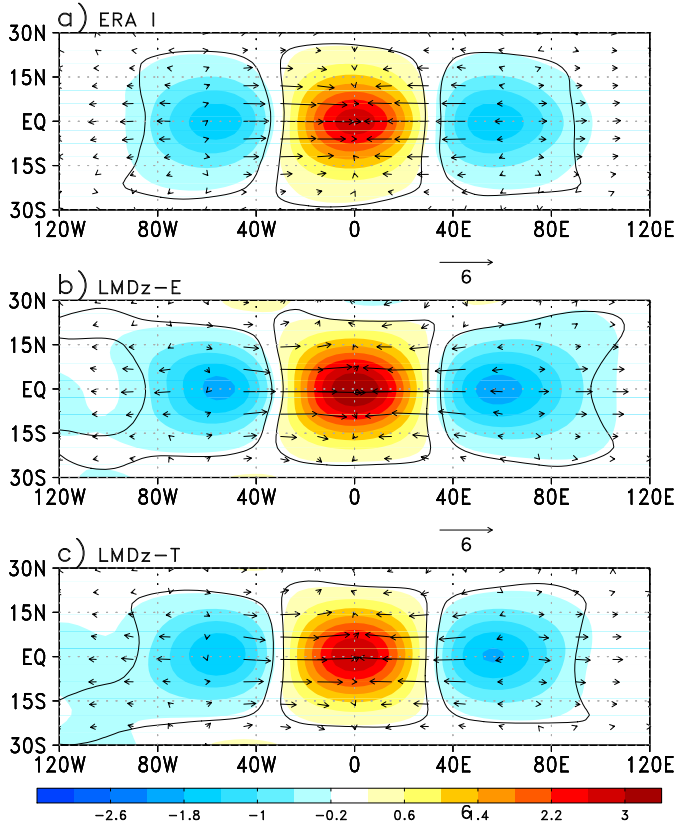

Fig. 6. Longitude–latitude maps for the KWs packets composite at the level $z_p = 50$ hPa and the $l = 0$day lag The shaded area are for the temperature T (red (blue) colours are for positive (negative) values, in K) and the arrows for the horizontal wind (u, v): **(a)** ERAI, **(b)** LMDz-E, and **(c)** LMDz-T. The black lines delimit the 99% significant regions according to a Student t test on the temperature.

ACPD
13, 22607–22637, 2013

On the presence of equatorial waves in the lower stratosphere

P. Maury and F. Lott

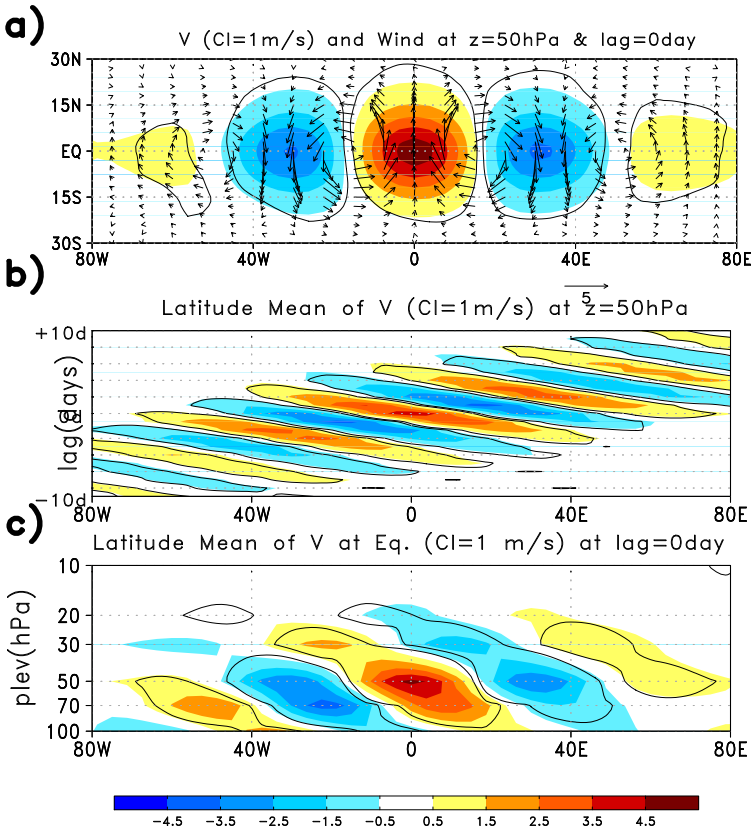

Fig. 7. RGWs composites from ERAI: **(a)** Meridional wind v (shading) and horizontal wind (u, v) (arrows) at z_p = 50 hPa and l = 0 day lag. **(b)** Hovmöller diagram of the meridional wind v at z_p = 50 hPa. **(c)** Longitude–altitude cross section of the meridional wind v averaged over the equatorial band. Shaded area are in red (blue) for positive (negative) values for meridional wind ($m s^{-1}$). The black lines delimit the 99 % significant regions according to a Student t test on the meridional wind.

ACPD
13, 22607–22637, 2013

On the presence of equatorial waves in the lower stratosphere

P. Maury and F. Lott

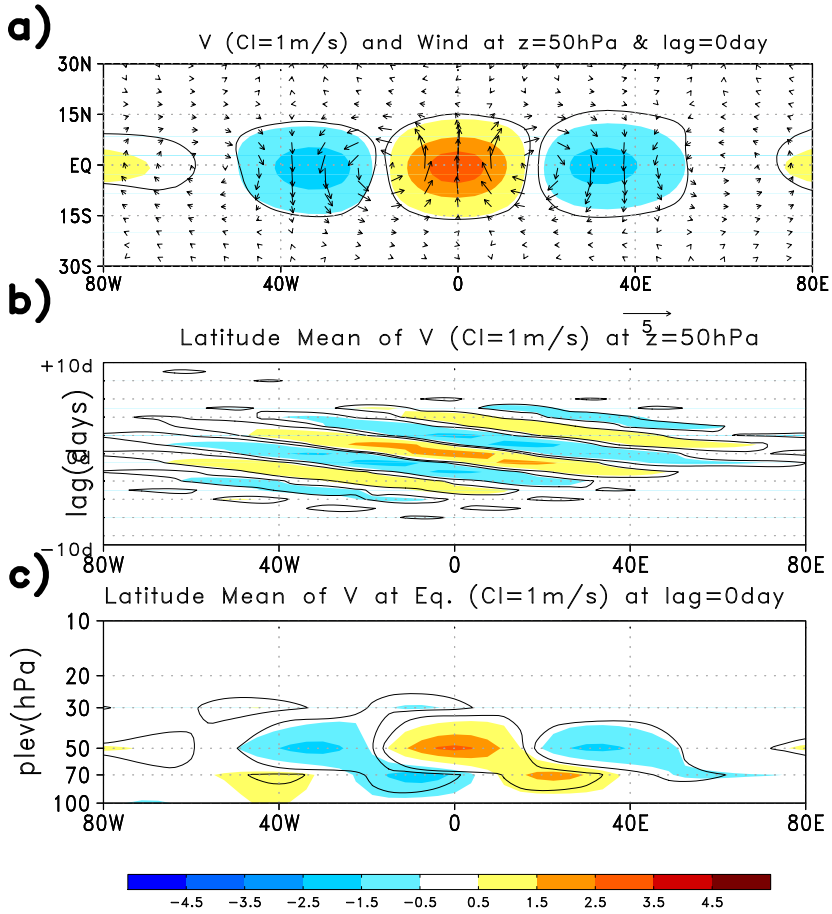

Fig. 8. Same as Fig. 7 for LMDz-E.

ACPD
13, 22607–22637, 2013

On the presence of equatorial waves in the lower stratosphere

P. Maury and F. Lott

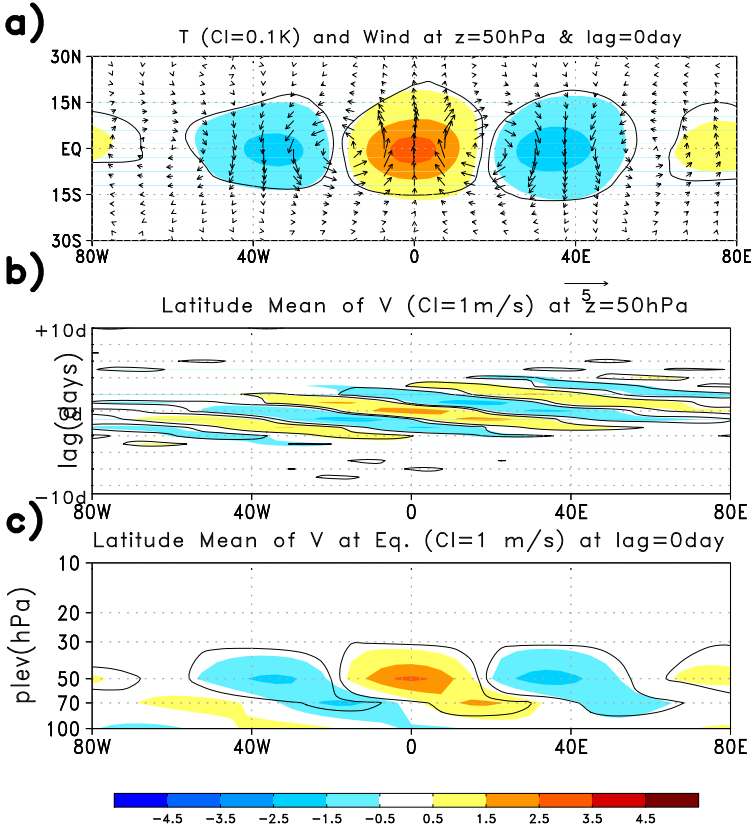

Fig. 9. Same as Fig. 7 for ERAI selecting dates when the zonal mean zonal wind is negative at 50 hPa.

ACPD
13, 22607–22637, 2013

On the presence of equatorial waves in the lower stratosphere

P. Maury and F. Lott

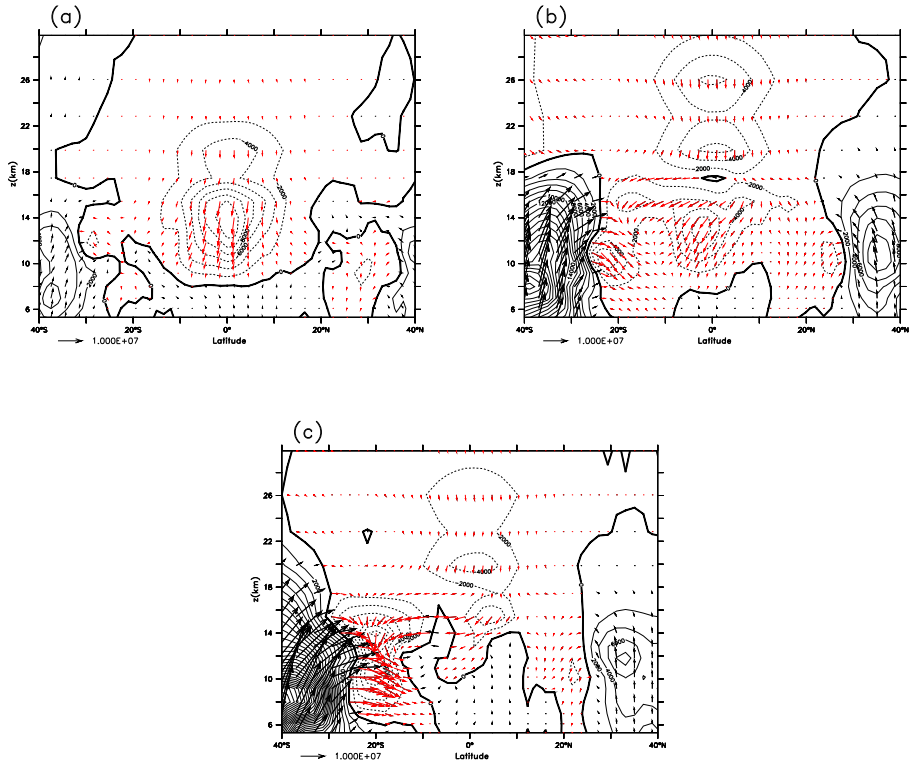

Fig. 10. Composite of the EP-flux vector $\left(\overline{F^{\phi}}, \overline{F^{z}}\right)$ (arrows) and of its vertical component $\overline{F^{z}}$ (contours with negative values dashed, interval of 1000 Pa, red (black) arrows corresponding to negative (positive) vertical component $\overline{F^{z}}$): **(a)** ERAI, **(b)** LMDz-E, **(c)** LMDz-T.

ACPD
13, 22607–22637, 2013

On the presence of equatorial waves in the lower stratosphere

P. Maury and F. Lott

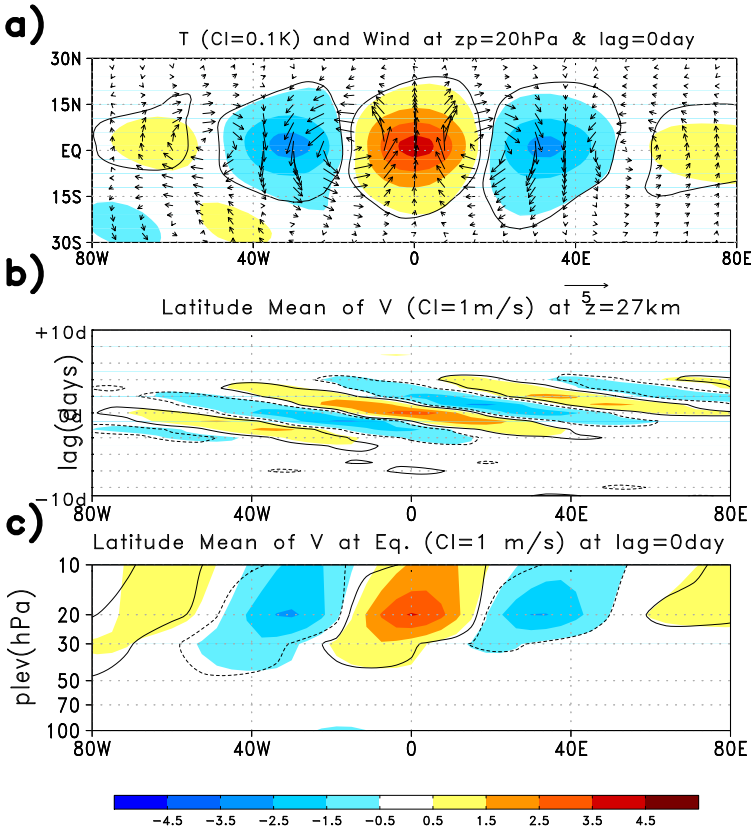

Fig. 11. Composite of the RGWs at 20 hPa calculated during negative phases of the QBO at 50 hPa (i.e., when the zonal wind is negative at 50 hPa and positive at 20 hPa) (red (blue) colours are for positive (negative) values). The black lines delimit the 99 % significant regions according to a Student *t* test on the meridional wind.

ACPD
13, 22607–22637, 2013